Nanoscale

Accepted Manuscript

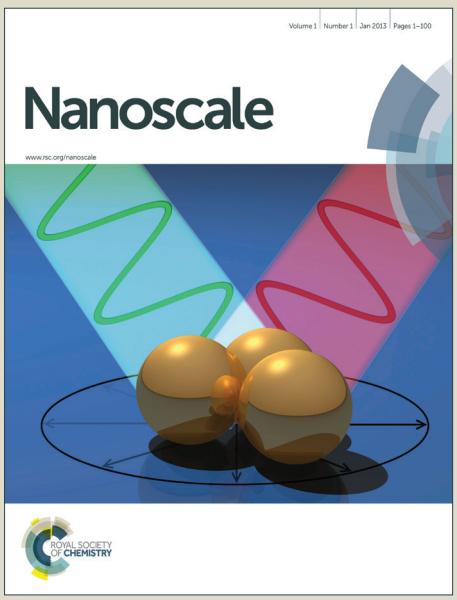

ROYAL SOCIETY OF CHEMISTRY

www.rsc.org/nanoscale

Journal Name

COMMUNICATION

Solvent Engineering Towards Controlled Grain Growth in Perovskite Planar Heterojunction Solar Cells

Received 00th January 20xx,
Accepted 00th January 20xx

DOI: 10.1039/x0xx00000x

www.rsc.org/

Yaoguang Rong,[a] Zhongjia Tang,[bc] Yufeng Zhao,[a] Xin Zhong,[b] Swaminathan Venkatesan,[a] Harrison Graham,[a] Matthew Patton,[d] Yan Jing,[a] Arnold M. Guloy,*[bc] and Yan Yao*[ac]

We report an effective solvent engineering process to enable controlled perovskite crystal growth and a wider window for processing uniform and dense methyl ammonium lead iodide ($MAPbI_3$) perovskite films. Planar heterojunction solar cells fabricated with this method demonstrate hysteresis-free performance with a power conversion efficiency around 10%. The crystal structure of an organic-based Pb iodide intermediate phase is identified for the first time, which is critical in controlling the crystal growth and optimizing thin film morphology.

Organic-based metal halide perovskites are a new family of optoelectronic materials that have attracted significant attention as light absorbers in efficient photovoltaic cells due to the unique combination of important characteristics such as a high extinction coefficient, long charge-carrier diffusion length, and low recombination rate along with a tunable bandgap.[1-16] Significant efforts have been expanded to investigate new organic-based perovskite materials such as methyl ammonium lead halides ($MAPbX_3$), different device architectures and efficient deposition methods for perovskite solar cells, leading to a remarkable power conversion efficiency (PCE) of 20.1%.[17-19] In conventional mesoscopic perovskite solar cells, a mesoporous metal oxide layer, such as TiO_2 and Al_2O_3, is employed as an electron accepting/transport or a scaffold layer, which requires a high-temperature (~500 °C) annealing step to make the fabrication process not only energy intensive but also incompatible with flexible plastic substrates.[3-5, 15-18] Planar heterojunction (PHJ) perovskite solar cells not only simplify the device fabrication but also enable low-temperature (<150 °C) solution processing. A typical PHJ perovskite solar cell has a *p-i-n* structure with the perovskite layer sandwiched between an electron transport layer (ETL) and a hole transport layer (HTL).[20-28]

In PHJ perovskite solar cells, the quality of the perovskite layer plays an important role in obtaining high PCE. One-step deposition,[16-18] two-step sequential deposition,[22-25] and vapor deposition[26, 27] have been developed to produce high-quality perovskite films. The simplicity of the one-step solution deposition approach makes it preferable to other methods due to potential fabrication cost reduction. Previous studies report inhomogeneous perovskite film coverage on flat substrates in the simple one-step spin-coating process, which results in insufficient light absorption as well as an increased charge carrier recombination rate, which causes a drop in both efficiency and yield.[17, 20, 28] Therefore, it is critical to optimize the film quality in the one-step deposition method with a deeper understanding of the film growth kinetics.

Solvent engineering has proven to be effective in fine-tuning the morphology of the pervoskite layer in one-step deposition for efficient solar cell devices.[17, 18] However, there remain two major challenges. First, when only a single solvent is used, the yield of high-quality dense film is low with a narrow processing window.[29] Second, an intermediate phase forms during the solvent treatment step, which plays a critical role in determining the pervoskite crystal growth. However, the crystal structure of the intermediate phase is still unknown.

Here we demonstrate a solvent-assisted film deposition method using a dimethylformamide/dimethyl sulfoxide (DMF/DMSO) solvent mixture, to enable a wider window for processing uniform and dense methyl ammonium lead iodide ($MAPbI_3$) perovskite films. We also determined the crystal structure of an organic-based Pb iodide intermediate phase for the first time. The novel film processing approach significantly improves the stability and reproducibility of the solvent treatment process. Moreover, the elucidation of the intermediate crystalline phase provides an improved understanding of the chemical processes involved in the film formation. Inverted perovskite/fullerene PHJ (P/F-PHJ) solar cells based on the structure of ITO/PEDOT:PSS/$MAPbI_3$/PCBM/Al are fabricated *via* solution processing at temperatures below 120 °C,

[a]*Department of Electrical and Computer Engineering and Materials Science and Engineering Program, University of Houston, Houston, Texas 77204, USA. Email: yyao4@uh.edu;*
[b]*Department of Chemistry, University of Houston, Houston, Texas 77204, USA. Email: aguloy@uh.edu;*
[c]*TexasCenter for Superconductivity at University of Houston, Houston, Texas, 77204, USA.*
[d]*Department of Chemical and Biomolecular Engineering, University of Houston, Houston, Texas 77204, USA.*
Electronic Supplementary Information (ESI) available: [Detailed experimental methods; photovoltaic performance of the devices; An X-ray crystallographic file (CIF).]. See DOI: 10.1039/x0xx00000x

Journal Name

COMMUNICATION

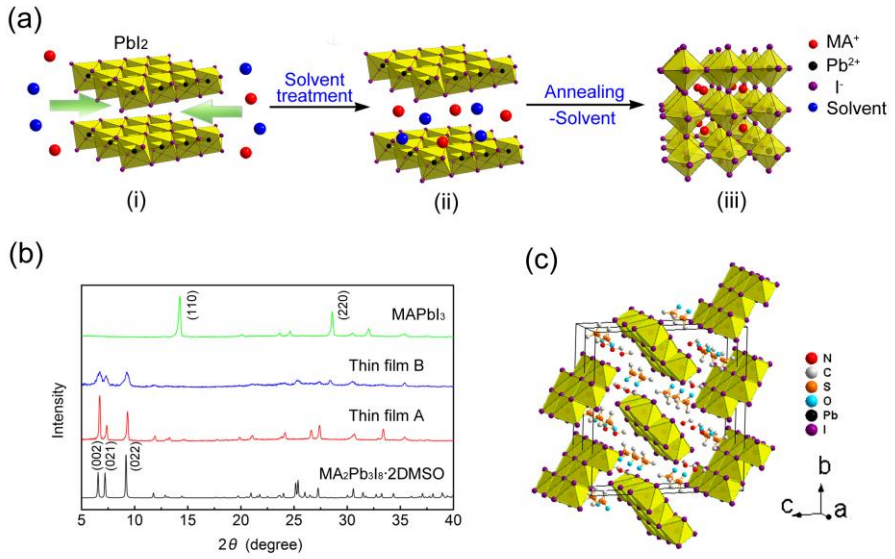

Figure 1. (a) Scheme of the $MAPbI_3$perovskite thin film forming process. (i) PbI_2 and MAI in the mixture solvent of DMF and DMSO; (ii) Exfoliation and intermediate phase formation after solvent treatment; (iii) $MAPbI_3$ perovskite thin film forms after thermal annealing. (b) XRD spectra of an intermediate single crystal $MA_2Pb_3I_8$·2DSMO, an intermediate from DMSO (thin film A), an intermediate phase from DMF/DMSO (thin film B), and an annealed perovskite film ($MAPbI_3$). (c) Crystal structure of $MA_2Pb_3I_8$·2DMSO.

resulting in a hysteresis-free photovoltaic performance and a PCE of ~10%.

Fig. 1 (a) presents the scheme for the $MAPbI_3$perovskite formation process. This process mainly consists of three steps: (i) PbI_2 and MAI are dissolved in mixture solvent and are then spun-cast on PEDOT:PSS coated ITO substrates at 5000 rpm; (ii) after spinning for a certain time, toluene was added as an orthogonal solvent for PbI_2 layers and the formation of an intermediate phase; (iii) the film was transformed to a final pervoskite phase after annealing at 100 °C for 15 minutes.

The key step in the above solvent engineering process is the formation of the intermediate phase. In previous work, the treatment process was found to be extremely sensitive to the delay time and resulted in a narrow processing window when DMF was used as the processing solvent.[29] In this work, DMSO was chosen as a co-solvent with DMF to gain the flexibility of tuning the coordination strength since DMSO has a stronger ability to coordinate with PbI_2 than DMF.[33, 34] Fig. 1b shows the XRD spectra of two intermediate phase films obtained from pure DMSO (thin film A) and from DMF/DMSO mixture solvents (thin film B). We observed the peaks located at 2ϑ = 6.61°, 8.12°, 9.63°, which agrees with previous report, however the crystal structure remains unknown.[17] To clearly understand the structure of the intermediate phase, single crystals of the phase were recrystalized and obtained from the mother liquor that forms the thin films. Single crystal X-ray diffraction was performed and showed the crystal structure is orthorhombic with space group *Cmc2₁* (No. 36). The crystallographic data is as follows: a = 4.621(1) Å, b = 27.484(8) Å, c = 26.923(7) Å, V = 3419.5(16) Å3; Z = 4; D_{calcd} = 3.607 g cm^{-3}. Final R indices [(I>2σ(I)]: R1 = 0.0538, wR2 = 0.1053. The crystal structure of the intermediate phase, as shown in Figure 1c features rib-bon-like chains, $[Pb_3I_8]^{2-}$, formed from edge-shared lead iodide octahedra (PbI_6). The $[Pb_3I_8]^{2-}$ ribbons, that run parallel with the a-axis, and can be depicted as excised ribbons from the layered PbI structure with widths of 3 octahedral PbI_6 units. The methylammonium (MA^+) and DMSO molecules are located in spaces between the ribbons. The DMSO molecules do not coordinate the Pb atoms of the $[Pb_3I_8]^{2-}$ ribbons, which is different when no MA^+ are present – i.e the coordination compound $PbI_2(DMSO)_2$ is formed.[17, 34] Crystal data and structure refinement results, as well as atomic coordinates and equivalent isotropic displacement parameters are listed presented in the supplementary information (Tables S1 and S2, respectively). The simulated powder XRD patterns based on the refined crystal structure (Fig.1b) matches nicely with the experimental X-ray diffraction pattern of the unannealed thin film samples (A&B). Upon thermal annealing the crystalline intermediate phase, $MA_2Pb_3I_8$·2DSMO, liberates DMSO and reacts with the residual MAI in the thin film to form

Journal Name

COMMUNICATION

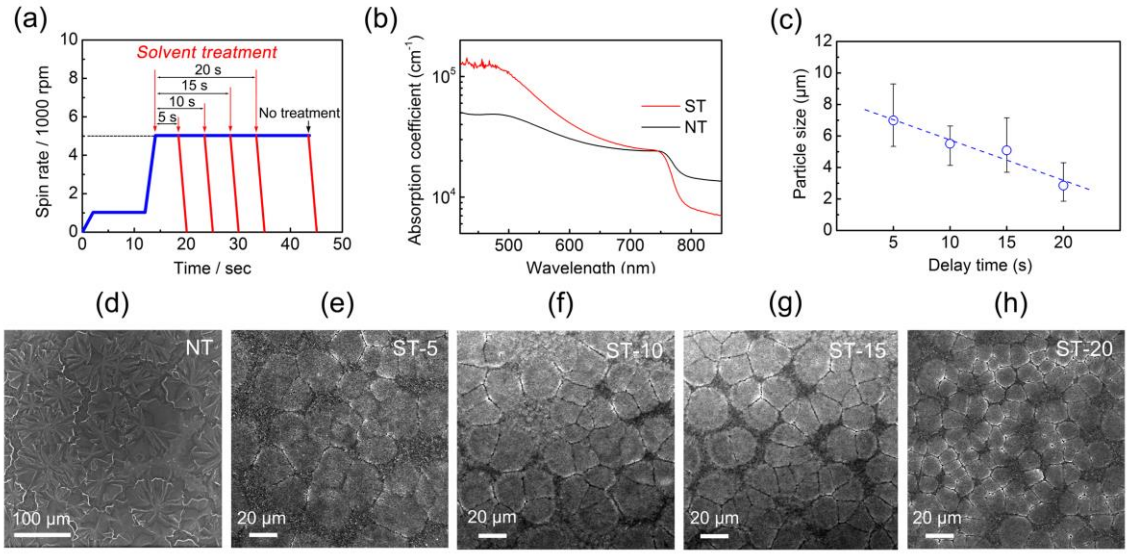

Figure 2. (a) The speed-time profile of spin-coating process for the solvent-assisted deposition method. For solvent treatment, the spin coating process stops immediately after adding solvent; For the process without solvent treatment, the 5000 rpm spin coating process lasts for 30 s. (b) UV-Visible spectra of $MAPbI_3$perovskite films deposited on PEDOT:PSS (~50 nm) coated ITO glass with solvent treatment (ST-10) and no treatment (NT); (c) Dependence of average grain size on delay time; (d-h) SEM images of $MAPbI_3$perovskite films deposited with NT (d) and delay time of 5 s (e), 10 s (f), 15 s (g) and 20 s (h).

tetragonal perovskite $MAPbI_3$, as shown in Figure 1b. The thermally activated transformation results in homogeneous and dense perovskite films. The presence of DMF or DMSO molecule in the intermediate phase film is further confirmed by Fourier transform infrared spectroscopy (FTIR) (Fig. S2). For the unannealed thin films A and B, the peak located at 1020 cm^{-1} is assigned to S=O stretching vibration of DMSO. After thermal annealing, the peaks originating from DMF or DMSO is significantly reduced, indicating the loss of solvent molecules and formation of $MAPbI_3$. Further understanding the crystal transformation of the intermediate phase $MA_2Pb_3I_8{\cdot}2DSMO$ will benefit the optimization of solvent engineering technique for obtaining high quality perovskite films.

In addition to the thermodynamics of the formation of intermediate phase, the kinetic aspects of the solvent treatment (ST) also significantly affect the film morphology. The parameters of detailed spin-coating process are presented in Fig. 2a. Toluene was dripped onto the film surface after a delay of 5 s (ST-5), 10 s (ST-10), 15 s (ST-15) and 20 s (ST-20) since the spin-coating step started at 5000 rpm. For the process with no treatment (NT), the spinning step continues at 5000 rpm for 30 s. Fig.2b compares the absorption curves for two films processed with and without solvent treatment. In the visible spectrum, treated film shows a significant higher absorption coefficient over 1×10^5 cm^{-1} in the range of 400-500 nm. In the above band-gap region, the scattering of treated film is considerably reduced compared to non-treated film, indicating enhanced uniformity of ST film. Fig. 2d-h show the surface morphology of pervoskite films processed at various conditions. When no solvent treatment was applied, the perovskite film presented a two-dimensional flower-like growth morphology (Fig. 2d) with crystal size between 50 to 80 μm. The gaps exist between perovskite grains will lead to reduced shunt resistance and leakage current. In comparison, as the treatment delay time increases from 5 s to 20 s, the average grain size reduced continuously from ~7 μm to ~3 μm (Fig. 2c). More importantly, the grains grow and merge together with much reduced gap region (darker region in Fig. 2e-h). In previously reported literature, the grain size was typically less than 1 μm.[17, 22, 24, 25] The much larger grain size reported in this work is significant in that it would enable the reduction of the overall bulk defect density and mitigate voltage hysteresis with suppressed charge trapping.[25, 35] Furthermore, decreasing the gaps between grains is expected to improve the quality of such large grains based perovskite films.

PHJ solar cells with a structure of ITO/PEDOT:PSS/$MAPbI_3$ (40 nm)/[6,6]-phenyl-C_{61}-butyric acid methyl ester (PCBM) (50 nm)/BCP (8 nm)/Al (100 nm) were fabricated and characterized under standard air-mass 1.5 global (AM 1.5G) illumination. The J-V curves for the devices fabricated with different delay time and measured with 50 ms scanning delay in reverse direction are presented in Fig. S3a. Table 1 summarizes the extracted parameters of open-circuit voltage (V_{oc}), short-circuit current density (J_{sc}), fill factor (FF) and

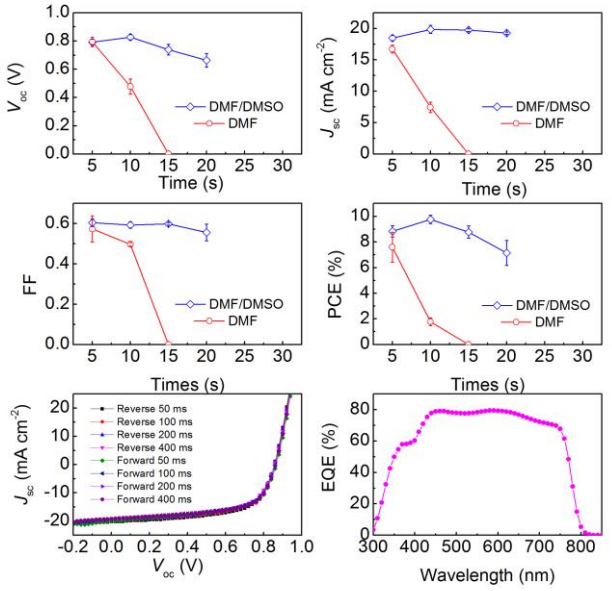

Figure 3. Variation of V_{oc} (a), J_{sc} (b), FF (c) and PCE (d) of the devices fabricated with different delay time and DMF/DMSO mixed solvents or pure DMF based precursor solution; (e) *J-V* curves of the device with optimal performance measured with different sweep delay time (50, 100, 200, 400 ms) and scan directions (Reverse scan: from 1.0 V to -0.2 V; Forward scan: from -0.2 V to 1.0 V); (f) EQE of the device.

PCE. In general, these devices present similar photovoltaic performance. A maximum PCE of 10.11% was obtained from device ST-10 due to the relatively higher V_{oc} (0.83 V) and Jsc (20.2 mA cm^{-2}) among all devices. The variations in the photovoltaic device parameters are plotted in Fig. 3a-d. For mixed solvents based devices, as the delay time increased from 5 s to 20 s, Voc of the devices increased slightly from 0.79 V to 0.83 V, and then decreased to 0.66 V. The change in V_{oc} could be related to the grain size variation. The larger grains reduces the total grain boundary area, which is expected to reduce the charge recombination at the grain boundaries thus improve the V_{oc}.[25, 35] Here it should be noted that though ST-5 film presented the largest grain size, the undesired large variation of grain size led to more unfavorable gaps between the particles, thus the ST-5 device has obtained a relative lower V_{oc}. Meanwhile, J_{sc} and FF of devices ST-5, ST-10 and ST-15 were not significantly affected by the delay time. In comparison to pure DMF solvent based devices, mixed solvents clearly enable a much longer processing window, which is related to the existence of the $MA_2Pb_3I_8$·2DSMO intermediate phase.

To investigate charge recombination in the devices, de-pendence of J_{sc} and V_{oc} on light intensity (I) was measured between 0.02 and 1.0 Sun. The J_{sc} and V_{oc} dependence on light intensity is plotted in Fig. S3b and c. For all devices, Jsc is linear with light intensity, indicating there is no significant charge recombination at short-circuit condition. For the V_{oc} of device ST-5, ST-10 and ST-15, the slopes of V_{oc}*vs*ln(I) are 0.057, 0.058 and 0.054, which are close to 0.052 ($2k_BT/q$), indicating the main recombination mechanism is monomolecular recombination.[36] For device ST-20, the slope is reduced to 0.042 ($1.6k_BT/q$), suggesting that recombination in this case is a combination of monomolecular and bimolecular processes.[37] The enhanced recombination is possible due to the reduced grain size in the ST-20 film.

Photocurrent hysteresis at certain sweep delay time and scan direction have been reported as a serious issue in perovskite solar cells.[38] The origin of photocurrent hysteresis is still under debate which may be due to either charge traps in low quality perovskite films, ferroelectric properties of the perovskite material, and/or the electromigration of ions in perovskites.[39] We measured the J-V curves of ST-10 using different sweep delay time (50, 100, 200, 400 ms, corresponding to scan rate of 400 mV s^{-1} to 50 mV s^{-1}) and scan directions (Reverse scan: from 1.0 V to -0.2 V; Forward scan: from -0.2 V to 1.0 V), as shown in Fig. 3e. Interestingly, no obvious photocurrent hysteresis at measured sweep delay time and scan directions were observed. This could be attributed to the high quality perovskite films with controlled grain growth, which benefits the charge transport and interface contact.[40, 41] Detailed photovoltaic parameters are summarized in Table S4, and the EQE data of the device is presented in Fig. 3f. This is very different from conventional planar structure and agrees with literatures on so-called reverse structured perovskite solar cells.[24, 25, 35, 40, 41]

Conclusions

A solvent-assisted film deposition method using a solvent mixture was developed and investigated in P/F-PHJ solar cells to enable wider processing window in forming uniform and dense perovskite films. The chemical process of the thin film deposition was studied, and a crystalline intermediate phase was identified and characterized. The morphology of the perovskite films and crystalline grain size were well controlled by the delay time in the solvent treatment process. A PCE of over 10% has been achieved for these devices without significant photocurrent hysteresis. These results provide important progress towards understanding the critical role of intermediate phases in the growth kinetics of pervoskite films and a better control of the solution-processing for low-cost and highly efficient perovskite solar cells.

ACKNOWLEDGMENT

Y.Y. acknowledges the TcSUH Welch Professorship Award and UH Startup fund. A. M. G. acknowledges the R. A. Welch Foundation (E-1297) and the State of Texas through the Texas Center for Superconductivity at the University of Houston.

Notes and references

1. A. Kojima, K. Teshima, Y. Shirai and T. Miyasaka, *J. Am. Chem. Soc.*, 2009, **131**, 6050-6051.
2. J. Im, C. Lee, J. Lee, S. Park and N. Park, *Nanoscale*, 2011, **3**, 4088-4093.
3. L. Etgar, P. Gao, Z. Xue, Q. Peng, A. K. Chandiran, B. Liu, M. K. Nazeeruddin and M. Grätzel, *J. Am. Chem. Soc.*, 2012, **134**, 17396-17399.
4. H. Kim, C. Lee, J. Im, K. Lee, T. Moehl, A. Marchioro, S. Moon, R. Humphry-Baker, J. Yum, J. E. Moser, M. Grätzel and N. Park, *Sci. Rep.*, 2012, , 591.
5. M. M. Lee, J. Teuscher, T. Miyasaka, T. N. Murakami and H. J. Snaith, *Science*, 2012, **338**, 643-647.
6. C. C. Stoumpos, C. D. Malliakas and M. G. Kanatzidis, *Inorg. Chem.*, 2013, **52**, 9019-9038.
7. G. Xing, N. Mathews, S. Sun, S. S. Lim, Y. M. Lam, M. Grätzel, S. Mhaisalkar,

and T. C. Sum, *Science*, 2013, **342**, 344-347.
8. E. Edri, S. Kirmayer, D. Cahen and G. Hodes, *J. Phys. Chem. Lett.*, 2013, **4**, 897-902.
9. S. D. Stranks, G. E. Eperon, G. Grancini, C. Menelaou, M. J. Alcocer, T. Leijtens, L. M. Herz, A. Petrozza and H. J. Snaith, *Science*, 2013, **342**, 341-344.
10. E. Mosconi, A. Amat, M. K. Nazeeruddin, M. Grätzel and F. De Angelis, *J. Phys. Chem. C*, 2013, **117**, 13902-13913.
11. J. H. Noh, S. H. Im, J. H. Heo, T. N. Mandal and S. I. Seok, *Nano Lett.*, 2013, **13**, 1764-1769.
12. G. E. Eperon, S. D. Stranks, C. Menelaou, M. B. Johnston, L. M. Herz and H. J. Snaith, *Energy Environ. Sci.*, 2014, **7**, 982-988.
13. W. J. Yin, T. Shi and Y. Yan, *Adv. Mater.*, 2014, **26**, 4653-4658.
14. M. A. Green, A. Ho-Baillie and H. J. Snaith, *Nat. Photonics*, 2014, **8**, 506-514.
15. Y. Rong, Z. Ku, A. Mei, T. Liu, M. Xu, S. Ko, X. Li and H. Han, *J. Phys. Chem. Lett.*, 2014, **5**, 2160-2164.
16. A. Mei, X. Li, L. Liu, Z. Ku, T. Liu, Y. Rong, M. Xu, M. Hu, J. Chen and Y. Yang, H. Han, *Science*, 2014, **345**, 295-298.
17. N. J. Jeon, J. H. Noh, Y. C. Kim, W. S. Yang, S. Ryu and S. I. Seok, *Nat. Mater.*, 2014, **13**, 897-903.
18. N. J. Jeon, J. H. Noh, W. S. Yang, Y. C. Kim, S. Ryu, J. Seo, S. I. Seok, *Nature,* 2015, **517**, 476-480.
19. W. S. Yang, J. H. Noh, N. J. Jeon, Y. C. Kim, S. Ryu, J. Seo, S. I. Seok, *Science*, 2015, DOI: 10.1126/science.aaa9272
20. J.-Y. Jeng, Y.-F. Chiang, M.-H. Lee, S.-R. Peng, T.-F. Guo, P. Chen and T.-C. Wen, *Adv. Mater.*, 2013, **25**, 3727-3732.
21. H. Zhou, Q. Chen, G. Li, S. Luo, T. Song, H. Duan, Z. Hong, J. You, Y. Liu and Y. Yang, *Science*, 2014, **345**, 542-546.
22. Y. Wu, A. Iislam, X. Yang, C. Qin, J. Liu, K. Zhang, W. Peng and L. Han, *Energy Environ. Sci.*, 2014, **9**, 2934-2938.
23. D. Liu, M. K. Gangishetty and T. L. Kelly, *J. Mater. Chem. A*, 2014, **2**, 19873-19881.
24. Z. Xiao, C. Bi, Y. Shao, Q. Dong, Q. Wang, Y. Yuan, C. Wang, Y. Gao and J. Huang, *Energy Environ. Sci.*, 2014, **8**, 2619-2623.
25. Z. Xiao, Q. Dong, C. Bi, Y. Shao, Y. Yuan and J. Huang, *Adv. Mater.*, 2014, **26**, 6503-6509.
26. D. Liu and T. L. Kelly, *Nat. Photonics*, 2014, **8**, 133-138.
27. M. Liu, M. B. Johnston and H. J. Snaith, *Nature*, 2013, **501**, 395-398.
28. G. E. Eperon, V. M. Burlakov, P. Docampo, A. Goriely and H. J. Snaith, *Adv. Funct. Mater.*, 2014, **24**, 151-157.
29. M. Xiao, F. Huang, W. Huang, Y. Dkhissi, Y. Zhu, J. Etheridge, A. Gray Weale, U. Bach, Y. B. Cheng and L. Spiccia, *Angew. Chem. Int. Ed.*, 2014, **126**, 10056-10061.
30. D. Shen, X. Yu, X. Cai, M. Peng, Y. Ma, X. Su, L. Xiao and D. Zou, *J. Mater. Chem. A*, 2014, **2**, 20454-20461.
31. P. A. Beckmann, *Cryst. Res. Technol.*, 2010, **45**, 455-460.
32. V. Mehrotra, S. Lombardo, M. O. Thompson and E. P. Giannelis, *Phys. Rev. B*, 1991, **44**, 5786.
33. A. Wakamiya, M. Endo, T. Sasamori, N. Tokitoh, Y. Ogomi, S. Hayase and Y. Murata, *Chem. Lett.*, 2014, **43**, 711-713.
34. H. Miyamae, Y. Numahata and M. Nagata, *Chem. Lett.*, 1980, 663-664.
35. W. Nie, H. Tsai, R. Asadpour, J.-C. Blancon, A. J. Neukirch, G. Gupta, J. J. Crochet, M. Chhowalla, S. Tretiak, M. A. Alam, H.-L. Wang, A. D. Mohite, *Science*, 2015, **347**, 522-525.
36. S. R. Cowan, A. Roy, A. J. Heeger, *Phys. Rev. B*, 2010, **82**, 245207.
37. L. J. A. Koster, V. D. Mihailetchi, R. Ramaker, P. W. M. Blom, *Appl. Phys. Lett.*, 2005, **86**, 123509.
38. H. J. Snaith, A. Abate, J. M. Ball, G. E. Eperon, T. Leijtens, N. K. Noel, S. D. Stranks, J. T.-W. Wang, K. Wojciechowski, W. Zhang, *J. Phys. Chem. Lett.*, 2014, **5**, 1511-1515.
39. E. L. Unger, E. T. Hoke, C. D. Bailie, W. H. Nguyen, A. R. Bowring, T. Heumüller,M. G. Christoforo, M. D. McGehee, *Energy Environ. Sci.*, 2014, **7**, 3690-3698.
40. J. H. Heo, H. J. Han, D. Kim, T. K. Ahn, S. H. Im, *Energy Environ. Sci.*, 2015, **8**, 1602-1608.
41. Y. Shao, Z. Xiao, C. Bi, Y. Yuan, J. Huang, *Nat. Commun.,* 2014, **5**, 5784.